



Coronal mass ejection hits mercury: A.I.K.E.F. hybrid-code results compared to MESSENGER data



W. Exner^{a,b,*}, D. Heyner^b, L. Liuzzo^d, U. Motschmann^{a,c}, D. Shiota^{e,f}, K. Kusano^e, T. Shibayama^e

^a Institute for Theoretical Physics, TU Braunschweig, Germany

^b Institute for Geophysics and Extraterrestrial Physics, TU Braunschweig, Germany

^c DLR Institute of Planetary Exploration, Berlin, Germany

^d School of Earth and Atmospheric Sciences, Georgia Institute of Technology, Atlanta, GA, USA

^e Institute for Space-Earth Environment Research, Nagoya University, Nagoya, Aichi, Japan

^f National Institute of Information and Communications Technology, Koganei, Tokyo, Japan

ARTICLE INFO

Keywords:

Plasma interaction

Mercury

Hybrid

Simulation

CME

ABSTRACT

Mercury is the closest orbiting planet around the sun and is therefore embedded in an intensive and highly varying solar wind. In-situ data from the MESSENGER spacecraft of the plasma environment near Mercury indicates that a coronal mass ejection (CME) passed the planet on 23 November 2011 over the span of the 12 h MESSENGER orbit. Slavin et al. (2014) derived the upstream parameters of the solar wind at the time of that orbit, and were able to explain the observed MESSENGER data in the cusp and magnetopause segments of MESSENGER's trajectory. These upstream parameters will be used for our first simulation run. We use the hybrid code A.I.K.E.F. which treats ions as individual particles and electrons as a mass-less fluid, to conduct hybrid simulations of Mercury's magnetospheric response to the impact of the CME on ion gyro time scales. Results from the simulation are in agreement with magnetic field measurements from the inner day-side magnetosphere and the bow-shock region. However, at the planet's nightside, Mercury's plasma environment seemed to be governed by different solar wind conditions, in conclusion, Mercury's interaction with the CME is not sufficiently describable by only one set of upstream parameters. Therefore, to simulate the magnetospheric response while MESSENGER was located in the tail region, we use parameters obtained from the MHD solar wind simulation code SUSANOO (Shiota et al. (2014)) for our second simulation run. The parameters of the SUSANOO model achieve a good agreement of the data concerning the plasma tail crossing and the night-side approach to Mercury. However, the polar and closest approach are hardly described by both upstream parameters, namely, neither upstream dataset is able to reproduce the MESSENGER crossing of Mercury's magnetospheric cusp. We conclude that the respective CME was too variable on the timescale of the MESSENGER orbit to be described by only two sets of upstream conditions. Our results suggest locally strong and highly variable dynamics of the CME on timescales of 15 min while MESSENGER was near closest approach.

1. Introduction

Mercury possesses a northward shifted, weak dipole field of 190 nT at its equator (Winslow et al., 2013). The dipole field is much weaker than anticipated from conventional dynamo theory and might be explained by a negative feedback effect from the magnetosphere on the interior dynamo process (Glassmeier et al., 2007; Heyner et al., 2011), a thin-shell model (Stanley et al., 2005) or a deep-seated dynamo process (Christensen, 2006). The interaction with the solar wind, deforms the internal

field into a magnetosphere qualitatively similar to that of the Earth but smaller in size. By analyzing magnetic field data from the MESSENGER spacecraft, Winslow et al. (2013) found that the average sub-solar bow-shock and magnetopause distances are about $2R_M$ and $1.5R_M$, respectively, where $R_M = 2440$ km is Mercury's planetary radius. Average solar wind conditions at Mercury's orbital distance of 0.4 AU result in particle density of $n_0 = 60 \text{ cm}^{-3}$, solar wind velocity of $u_0 = 350 \text{ km/s}$ and a ram pressure of $p_{\text{ram},0} = 14.2 \text{ nPa}$ which yields an average Alfvén Mach number of $M_{A,0} = 6.6$ (Winslow et al., 2013). Apart

* Corresponding author. Institute for Theoretical Physics, TU Braunschweig, Germany.
E-mail address: w.exner@tu-bs.de (W. Exner).

from the Alfvén Mach number and the solar wind dynamic pressure, the overall appearance of the magnetosphere depends strongly on the orientation of the interplanetary magnetic field (IMF). On the basis of MESSENGER data, the variability of the IMF at Mercury's orbit is discussed by Baker et al. (2011) and Korth et al. (2011).

Variability of the IMF at Mercury's orbital position has been observed by the MESSENGER spacecraft during the first three MESSENGER flybys at Mercury, where the IMF orientation was northward (M1), southward (M2) or combination of the two (M3), leading to significantly different structures of Mercury's magnetosphere as discussed by Slavin et al. (2012); Raines et al. (2011). Further analysis of MESSENGER data was performed to determine solar wind conditions for M1 by Benna et al. (2010), who used a two fluid approach to model magnetometer (MAG) data. The differences in the magnetospheric structures between northward and southward IMF observed during M1 and M2 were addressed by means of hybrid (kinetic ions, fluid electrons) simulations by Trávníček et al. (2010) and Hercík et al. (2013). Additional hybrid simulation studies were carried out by Wang et al. (2010), who studied Mercury's magnetosphere with respect to the different IMF orientations during M1 and M2, and also compared their results with MESSENGER MAG data. Müller et al. (2012) used the A.I.K.E.F. (Adaptive Ion-Kinetic Electron-Fluid) hybrid code, the same that is used in the present study, to analyze a “double magnetopause” structure observed during M1 and M2 and demonstrated that a current sheet feature corresponding to the double magnetopause arises from trapped solar wind particles that are injected into the magnetosphere by night-side reconnection events. By using a two layer approach consisting of a high conducting core and low conducting mantle, Jia et al. (2015) showed that induction effects can have significant impact on the global interaction.

Although its structure has been extensively investigated for a large variety of solar wind conditions, a comprehensive understanding of Mercury's magnetosphere based on MESSENGER data is far from complete. Because the time-scale of the response of Mercury's magnetosphere to a change in the solar wind Mercury is tied to the Dungey scale (on the order of 2 ± 1 min (Slavin et al., 2009, 2010)), any changes in the solar wind on the time-scale of a few minutes should have a drastic influence on the appearance of Mercury's magnetosphere.

The response of Mercury's magnetosphere to a CME is even more extreme than its response to the average variability of the solar wind. The impact of a CME can be evaluated by two approaches. First by checking

the magnetic disturbance index (Anderson et al., 2013) and second by evaluating the magnetic field perturbations just within the day-side magnetopause when an increase over 300 nT on the day-side magnetosphere occurs. The second approach has only been reported on three occasions in MESSENGER data: two of which were CME events while the other was a high-speed stream occurrence (Slavin et al., 2014). The MESSENGER magnetic field measurements during these events had a magnetic disturbance index of 99.9, 100 and 92.9, respectively, indicating that Mercury's magnetosphere was highly perturbed (Anderson et al., 2013). In this study we focus on the first CME event that was observed in MESSENGER MAG data, which occurred during orbit 503 on 23 November 2011 as an example to determine how the magnetosphere of Mercury reacts to extreme upstream conditions. The magnetic field measurements from this orbit along with the two orbits before and the two orbits after are shown in Fig. 1 with black and green lines respectively, while the pink, turquoise and yellow areas indicate the segments where MESSENGER was inside the magnetosphere, magnetosheath and solar wind respectively. Analyzing the shortly constant upstream solar wind after the final bow-shock crossing, one set of upstream parameter has been derived to explain the whole MESSENGER data set (Slavin et al., 2014).

For this study, we employ the hybrid simulation code A.I.K.E.F. for accurate modeling of the solar wind interaction with Mercury. We will show how drastically the solar wind parameters change from one regime to another within a timescale of 15min and discuss important current systems as well as changes in the global configuration of Mercury's magnetosphere as it responds to these highly variable upstream conditions. We conclude that the given parameter set explains day-side measurements but not cusp data or night-side data. Further parameter sets are necessary for a full explanation of MESSENGER data.

This paper consists of four sections, namely: Section 2 will explain the motivation and method used to obtain input parameters for our simulations. Section 3 will introduce the A.I.K.E.F. model and the Space-weather-forecast-Usable System Anchored by Numerical Operations and Observations, Solar Wind model code (SUSANOO, Shiota et al. (2014), Shiota and Kataoka (2016)). A short overview of the numerical parameters and physical upstream conditions used as input to these simulation codes are also included in this section. Section 4 will focus on MESSENGER data of the magnetosphere's response to the CME that occurred on 23 November 2011, by using the values given by Slavin et al.

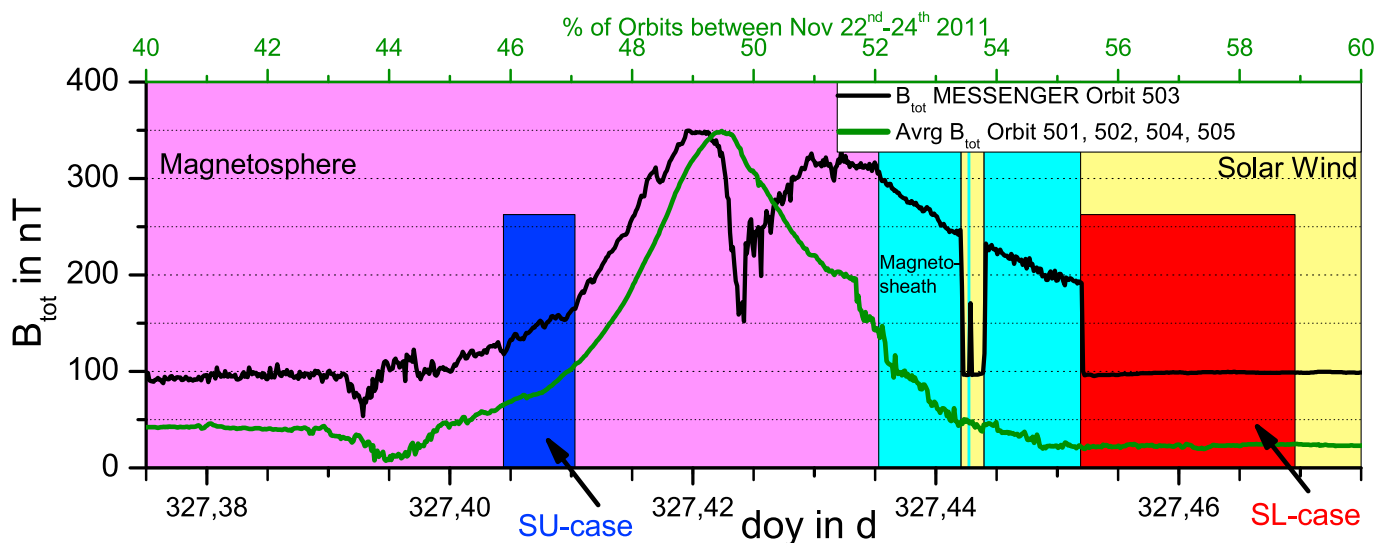


Fig. 1. Total magnetic field measurements over a percentage of the given MESSENGER orbit. The black line shows the measurements for orbit 503 on 23 November 2011. The green line shows the averaged measurements of orbits 501, 502, 504 and 505. The pink, turquoise and yellow areas show the segments where MESSENGER was inside the magnetosphere, magnetosheath and solar wind respectively. The red and blue areas denote the time ranges used for the solar wind upstream parameters for the A.I.K.E.F. hybrid simulations, where the SL-parameters have been obtained by MESSENGER MAG data (Slavin et al., 2014) and the SU-parameters have been simulated by the solar wind MHD code SUSANOO (Shiota et al., 2014).

(2014) and SUSANOO for our A.I.K.E.F. code. Comparing the simulation results to MESSENGER data will give us an insight into the variability of the CME. We discuss the response of important current systems near Mercury, as well magnetospheric regions such as the bow-shock, cusp region and plasma sheet. In that section, we first introduce the global 3D structure of the magnetosphere and the main features of the associated current systems. Then, a 2D view of the equatorial and MESSENGER orbital planes will be presented, where we investigate the structure of Mercury’s upstream bow-shock, cusp region and plasma sheet. Lastly, we compare direct simulation output from the model along the MESSENGER trajectory with in-situ measurements. We conclude with a summary and discussion of the key results in section 5.

2. Parametrization of the CME

Because of an absence of a stationary monitor between the Sun and Mercury, it is challenging to obtain parameters of the upstream solar wind or properties of the highly dynamic CME that passed Mercury. While multiple monitors on satellites around Earth allow for a global mapping of solar wind data, the solar wind and CME interaction with the Earth’s magnetosphere is understood much better than the situation at

Mercury. Even though the magnetosphere of Mercury is similar to Earth’s in shape, its size is tiny in comparison (see e.g. Winslow et al. (2013)). Additionally, because of its vicinity to the Sun of 0.4 AU, CMEs are stronger and more violent compared to Earth, located at an orbital distance of 1 AU. Thus, the interaction of Mercury’s magnetosphere with CMEs is in need of further investigation.

The only long term satellite mission to study Mercury has been MESSENGER, whose orbit was highly eccentric and, for our researched time interval, was embedded inside the upstream solar wind for only small fractions of time (see Fig. 1 which shows magnetometer data from a select few MESSENGER orbits, and upper right panel of Fig. 2 which shows a schematic of a single MESSENGER orbit). Therefore obtaining information about the solar wind upstream conditions over the timescale of an entire orbit is very difficult.

To motivate our approach of parameterizing an incoming CME, we sketch the possible magnetic field behavior of a CME measured by a hypothetical stationary monitor S (see upper right panel of Fig. 2) between the Sun and Mercury as given in the upper left Fig. 2. In this figure, the CME is divided into three segments, namely PRE-CME, CME-Phase and POST-CME. PRE- and POST-CME are governed by a somewhat constant, undisturbed solar wind as the real MESSENGER measurements

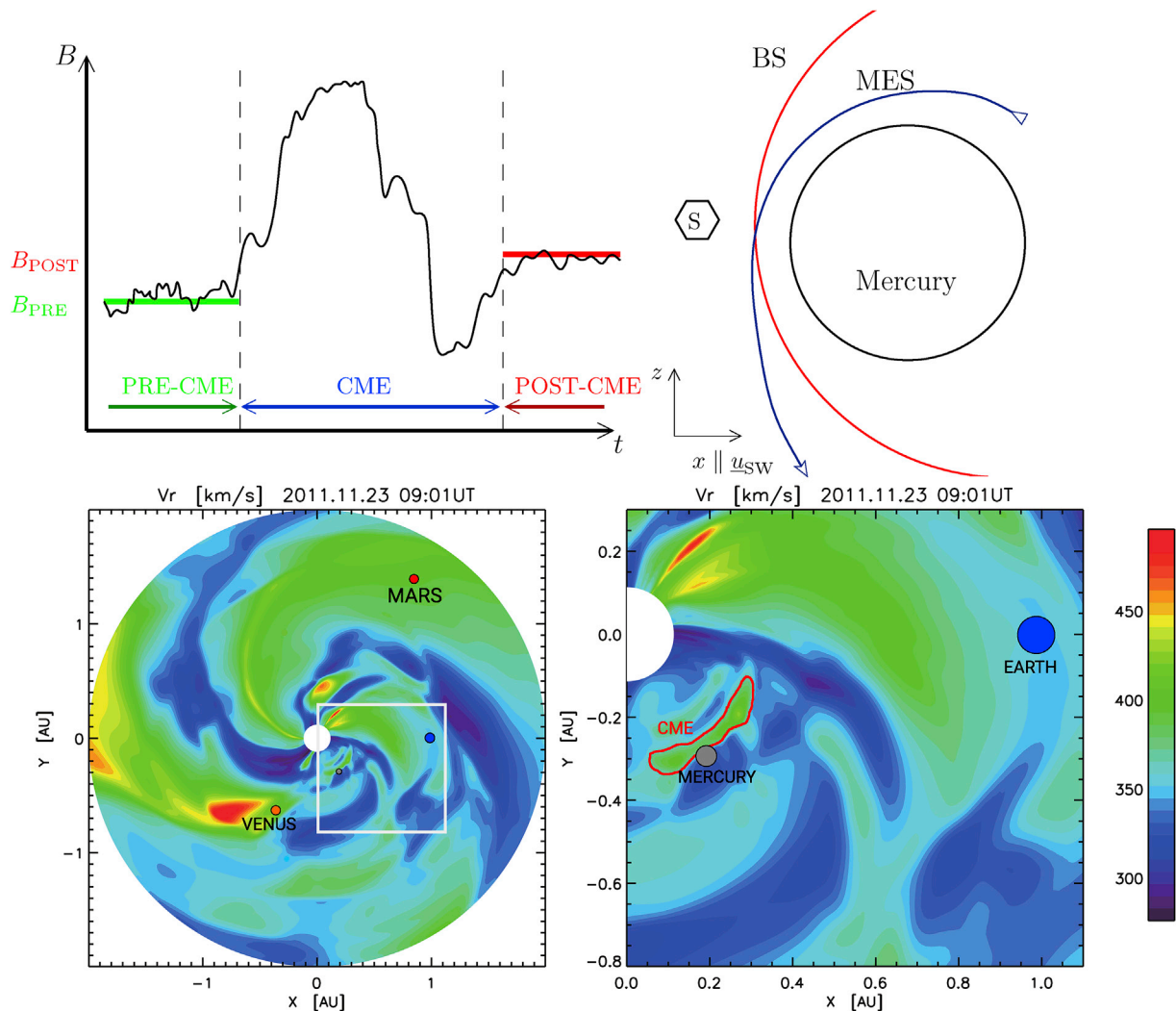


Fig. 2. Upper left: Hypothetical magnetic field measurements of a CME at monitor S (upper right panel) over time. The hypothetical measurements are divided into three sections, denoted “PRE-” and “POST-CME” with calm, undisturbed solar wind conditions, and a more violent “CME”-phase in the middle. Upper right: Sketch of Mercury (black) with its bow-shock (red). The hexagon shows a possible position of a magnetometer S that only measures upstream solar wind, while MESSENGER (blue) measures inside the magnetosphere for a long part of its orbit around Mercury. Bottom: Solar wind velocity distribution in km/s inside the ecliptic plane for the SUSANOO simulation of the CME. The CME hits Mercury directly upfront in the ecliptic plane. The sizes of the planets are not to scale.

inside the red rectangle in Fig. 1 also suggest. Combined with the measured increased upstream magnetic field compared to the averaged magnetic field in Fig. 1, it is likely that MESSENGER observed a POST-CME magnetic field. If we could only choose one parameter to approximate the CME-Phase magnetic field, then after our sketch, the magnetic field of B_{POST} is stronger and therefore closer to describe the CME-Phase, than the previous B_{PRE} .

Thus, for a first-order approximation of Mercury's magnetospheric response to the CME, we will use the parameters given by Slavin et al. (2014) as input for our simulations, the POST-CME-phase simulation. To obtain the parameters of the CME inside the CME-Phase, when MESSENGER was still inside Mercury's magnetosphere, we use the monitor S at the location between the Sun and Mercury that is fed by solar wind parameters given by the SUSANOO solar wind model, which is described briefly in the next section.

The SUSANOO model results for the velocity distribution of the CME on 23 November 2011 are displayed in the lower Fig. 2 and show that the CME hits Mercury directly with its frontal shock in the ecliptic plane.

The Dungey-cycle time-scale at Mercury is in the order of 2 min (Slavin et al., 2009, 2010), resulting in a nearly adiabatic response of Mercury's magnetosphere to changing upstream conditions. Therefore, we represent the magnetic field of the incoming CME as piece-wise, with a set of two upstream parameters.

3. Hybrid code A.I.K.E.F. and simulation parameters

To study the interaction of a coronal mass ejection with Mercury's magnetosphere, we apply the A.I.K.E.F. simulation code (Müller et al., 2011). As a hybrid code, it describes the ions as particles that can move within the cells of our simulation mesh. Electrons, in contrast, are handled as a mass-less charge-neutralizing fluid. A.I.K.E.F. has already been successfully applied to Mercury's plasma interaction by Müller et al. (2012) and Wang et al. (2010). Furthermore, A.I.K.E.F. has been used to study the interaction scenarios of many solar system bodies, such as the plume of Saturn's moon Enceladus (Kriegel et al., 2014) and atmosphere of Titan (Feyerabend et al., 2016), comet 67P/Churyumov-Gerasimenko, the target of the Rosetta mission (Koenders et al., 2015) as well as the induced dipole at the Jovian moon Callisto (Liuzzo et al., 2016). The model equations and the implementation of A.I.K.E.F. are described in great detail in the aforementioned studies, so only a discussion of parameters applicable to Mercury's magnetosphere are reported here.

In this study, we use the Mercury Anti Solar Orbital (MASO) coordinate system in which the x -axis is aligned with the solar wind. The y -axis points in the direction of Mercury's orbital motion and the z -axis completes the right-handed system, thereby pointing northward. MESSENGER MAG data has been transformed to fit the MASO coordinate system as well. Our goal is to understand the physics of the MESSENGER data-set when MESSENGER is close to the magnetopause and bow-shock region of Mercury's magnetosphere. The simulation box is spacious enough to fit MESSENGER's orbit inside, with a size of $L_x \times L_y \times L_z = 12R_M \times 6R_M \times 12R_M$ (see Table 1 for a summary of the numerical parameters) and with Mercury at the origin $\mathbf{0} = (0.35 L_x, 0.50 L_y, 0.65 L_z)$. A hierarchical mesh with three levels of refinement (L_0, L_1, L_2) that is adaptive in space but static in time is used. At the coarsest level (L_0), the resolution Δ is $\Delta_{L_0} = 140 \text{ km} = 0.058R_M$, while $\Delta_{L_2} = \frac{1}{4}\Delta_{L_0} = 35 \text{ km} = 0.014R_M$ is achieved at the highest level. In each cell, the ions are represented by about 20 macroparticles with the same charge-to-mass ratio as solar wind protons, yielding a total of more than 1.5 billion macroparticles in the plasma simulation. With a time step of 0.0025 gyroperiod (Ω_0^{-1}), the simulation becomes quasi-stationary after about 80 000 time steps, i.e. after $200 \Omega_0^{-1}$ or about 340 s. To improve stability of the simulation, a smoothing with a strength of 5% is applied to the electromagnetic fields (Müller et al., 2011). Mercury itself is modeled by a perfectly conducting core with a size of $0.8R_M$ (Smith et al., 2012; Hauck et al., 2013; Johnson et al., 2016) surrounded by a nearly insulating mantle with a resistivity of

Table 1

Solar wind parameter used as input for the A.I.K.E.F. hybrid simulations. Physical parameters of Mercury are obtained from Anderson et al. (2012) and Winslow et al. (2013).

Parameter	Value Slavin	Value SUSANOO
Magnetic field strength	$B_{0,SL} = 97 \text{ nT}$	$B_{0,SU} = 5.5 \text{ nT}$
Magnetic field direction	$\underline{B}_{0,SL} = (-7.66, -92.0, 31.9)$	$\underline{B}_{0,SU} = (1.3, 5.2, -1.25)$
Solar wind velocity	$u_{0,SL} = 450 \text{ km/s}$	$u_{0,SU} = 360 \text{ km/s}$
Solar wind number density	$n_{0,SL} = 140 \text{ cm}^{-3}$	$n_{0,SU} = 193 \text{ cm}^{-3}$
Alfvén Mach number	$M_{A,SL} = 2.5$	$M_{A,SU} = 42$
Ion mass		$m_i = 1 \text{ amu}$
Ion temperature		$T_i = 2 \cdot 10^5 \text{ K}$
Electron temperature		$T_e = 2 \cdot 10^5 \text{ K}$
Radius of Mercury		$R_M = 2440 \text{ km}$
Resistivity of mantle		$\eta = 1.2 \cdot 10^7 \Omega \text{m}$
Core size		$0.8R_M$
Dipole moment		$190 \text{ nT } R_M^3$
Dipole offset		480 km
Box (x)		$-4R_M \leq x \leq +8R_M$
Box (y)		$-3R_M \leq y \leq +3R_M$
Box (z)		$-8R_M \leq z \leq +4R_M$
Highest resolution		$\Delta_{L_2} = 35 \text{ km} = 0.014R_M$
Time step		$\Delta t = 0.0025\Omega_i^{-1} = 4.25 \cdot 10^{-3} \text{ s}$
Simulation time		$\tau = 8 \cdot 10^4 \Delta t = 200\Omega_i^{-1} = 340 \text{ s}$
Smoothing		$\eta_{sm} = 5\%$

$\eta = 1.2 \cdot 10^7 \Omega \text{m}$ (Jia et al. (2012), Anderson et al. (2011)). For increased numerical stability, the resistivity gradient at the inner and outer edge of the mantle is slightly smoothed (see Müller et al. (2012) and Vernisse et al. (2017)). In consequence this results in a smoothed resistivity profile similar to that used by Jia et al. (2015).

In the simulation a vacuum forms in Mercury's wake that would stop our hybrid code from functioning. Thus, ghost protons with a density of $10^{-3}n_0$ are injected into the potential vacuum regions at each time step to prevent the code from crashing but these have no significant impact on the solar wind particles of density n_0 .

MESSENGER data from orbit 503 on 23 November 2011 show a dramatic increase in magnetic field strength compared to the two preceding and two subsequent orbits (see Fig. 1). Slavin et al. (2014) analyzed the magnetic field measurements and found four bow-shock crossings within 15min, displaying a jump-strength of 100 nT. Those authors attributed these high internal variations to an incoming CME. To estimate the constant solar wind parameters after the final bow-shock crossing that occurred at 54.4% of the orbit (or 10:51:30 UTC, or 327.4525 doy), Slavin et al. (2014) averaged the values from within the red rectangle in Fig. 1 as listed in Table 1 with the subscript SL.

With the SUSANOO model (Shiota et al., 2014), we can obtain a global MHD simulation of the solar wind and the propagation of CMEs in the inner heliosphere up to 2 AU. The solar wind is simulated by observations of the sun's surface, while the CME's parameters are additionally derived from observations of the solar corona. The observations of timing, velocity, direction, shape, orientation and its magnetic structure (introduced in Shiota and Kataoka (2016)) are specified by the SOHO LASCO CME catalog (Yashiro, 2004) and its associated solar flare. With these parameters, the CME is modeled with a magnetic fluxrope (Shiota and Kataoka, 2016). Thus, the propagation into the heliosphere can be obtained. The magnitude and direction of the IMF within the fluxrope can therefore be reproduced during a given CME passage at Mercury. This method is an improvement over non-fluxrope solar wind codes (cf. Baker et al. (2013)). However, differences between simulated and measured IMF are due to longer distances between the solar surface and Mercury.

With the SUSANOO code, we are able to obtain simulated solar wind data between 327.405 doy and 327.41 doy of the orbit when MESSENGER was located within the night-side magnetosphere of Mer-

cury denoted by the blue rectangle in Fig. 1.

The parameters of the CME model used in this study are included in Table 2, which are also shown in the SOHO LASCO CME catalog (Yashiro, 2004). The velocity output within the ecliptic plane of the SUSANOO model for these parameters is shown in the bottom Fig. 2. The simulated CME hits Mercury directly upfront at the same time as MESSENGER data indicates and therefore validates the interpretation of an existing CME within MESSENGER observations. The values obtained from SUSANOO are included in Table 1 with the subscript SU.

4. Comparison of the A.I.K.E.F. simulation results to MESSENGER observations

4.1. 3D-section: global appearance of Mercury's magnetosphere

Magnetometer observations on 23 November 2011 suggested that a CME passed over the planet during MESSENGER orbit 503. The parameters of the solar wind for this simulation obtained from within the short duration of constant solar wind after the MESSENGER's final bow-shock crossing (see Fig. 1). From this POST-CME phase, the SL-parameters of the solar wind result in a super-sonic plasma with an alfvénic mach number of $M_{A,SL} = 2.5$, a magnetic field strength of $B_{0,SL} = 97$ nT, a particle density of $n_{0,SL} = 140 \text{ cm}^{-3}$ and a solar wind velocity of $u_{0,SL} = 450$ km/s (see Table 1).

The SU-parameters give a magnetic field strength of $B_{0,SU} = 5.5$ nT, a solar wind velocity of $u_{0,SU} = 360$ km/s and a particle density of $n_{0,SU} = 193 \text{ cm}^{-3}$, thus yielding an alfvénic mach number of $M_{A,SU} = 42$.

Using the SL- and SU-parameters, the simulations with our A.I.K.E.F. code yield vastly different responses of the magnetosphere of Mercury. These configurations are presented in Figs. 3, 4 and 5 where the top subfigures show the simulation with the SL-parameters and the bottom with the SU-parameters.

In these figures, Mercury is shown as a grey sphere surrounded by white magnetic field lines. The orange line shows the projection of MESSENGER's orbit on Mercury's surface. MESSENGER's orbit is shown by orange, blue and red points to distinguish between upstream, northern polar and tail region sections of the orbit respectively. For easier viewing, green and blue planes have been included to show the (001)-xy-plane ($z=0$) and (100)-yz-plane ($x=0$) (whereas xyz denote the Miller indices i.e. directions of the vector normal to the respective plane). The global configuration of the magnetosphere of Mercury is shown via magnetic field lines, regions of maximal particle density and the current system in Figs. 3, 4 and 5 respectively.

The magnetic field lines in the SL-case show a relaxed structure compared to the violent SU-situation. MESSENGER's orbit is barely inside the cusp region in the SL-case and only grazes the dawn side of the cusp in the SU-case. Many field lines near to the magnetopause are twisted and curved due to the different magnetic field orientation of the solar wind and its high mach number of the SU-case of $M_{A,SU} = 42$ compared to $M_{A,SL} = 2.5$ in the SL-case.

Similar behavior is seen in the particle density. In the SL-case the

density increases with $n > 3.5n_0$ (due to the bow-shock) and has a tidy appearance compared to the SU-situation. Additionally, only the SL-case shows a high density increase inside the cusp region where particles flow towards the surface of Mercury. The bulk-density is only slightly encountered by the MESSENGER orbit.

From the orientation of the magnetic field lines, our simulations show that the current systems generating the magnetic perturbations are wildly different between the two input parameters. The currents in the bow-shock regions (plotted within the green plane) flow in nearly opposite directions. The magnetopause current in the SU-case flows around Mercury perpendicular to the local magnetic field lines. Unexpectedly, the current within the magnetopause in the SL-case is closely field

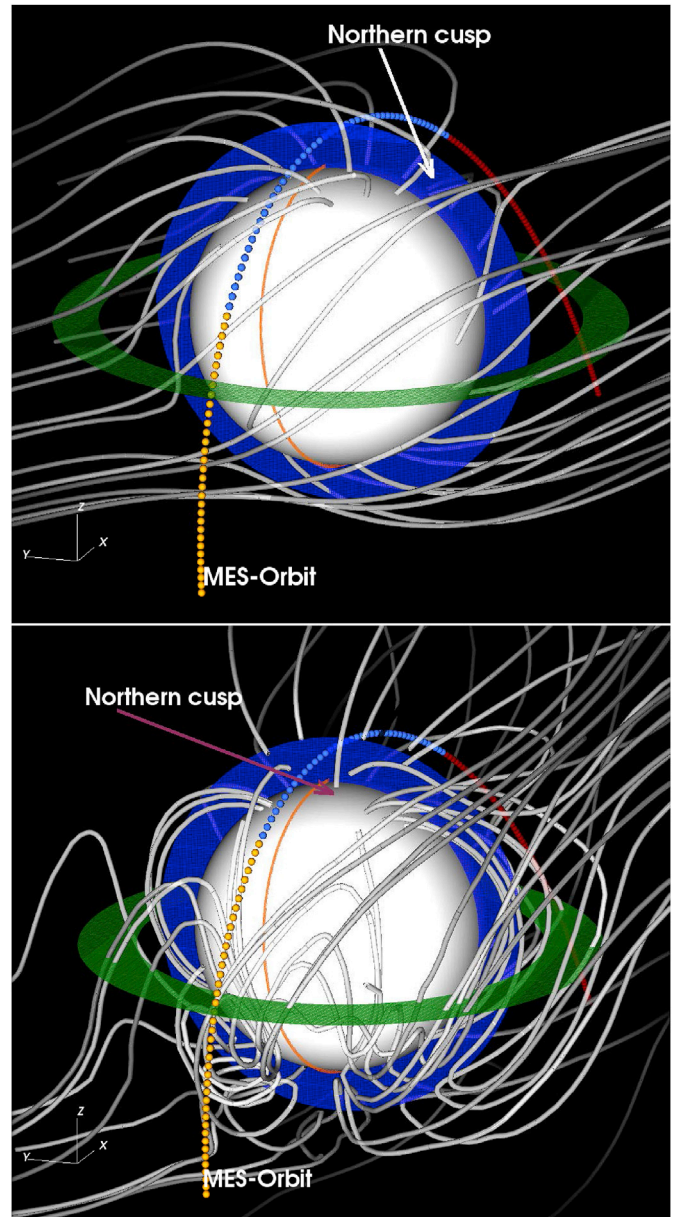


Fig. 3. Top: Results of the global hybrid simulation using upstream parameters obtained from Slavin et al. (2014). Bottom: Results of the global hybrid simulation using upstream parameters obtained from SUSANOO. Depicted in green and blue are the xy- and xz-planes respectively. The MESSENGER orbit is displayed with orange, blue and red points to distinguish the orbit segments inside the solar wind, the northern polar and the tail region, respectively. The orange line visible on Mercury's surface indicates the projection of MESSENGER's orbit. Magnetic field lines are shown by white tubes.

Table 2

Numerical parameters used for the SUSANOO MHD simulations shown in the lower Fig. 2. For a more detailed description of the parameters see Shiota and Kataoka (2016).

Parameter	Value SUSANOO
Heliographic latitude of source	12°
Heliographic longitude of source	-49°
Tilt of CME	180°
Velocity of CME	506 km/s
Torodial Flux of CME	$1.0 \cdot 10^{20}$ Mx
Radial width of CME	2 RS
Angular width of CME	60°
Chirality of twist in CME	1
Time YYYY.MM.DD.HH.MM.SS	2011.11.22.4.0.0

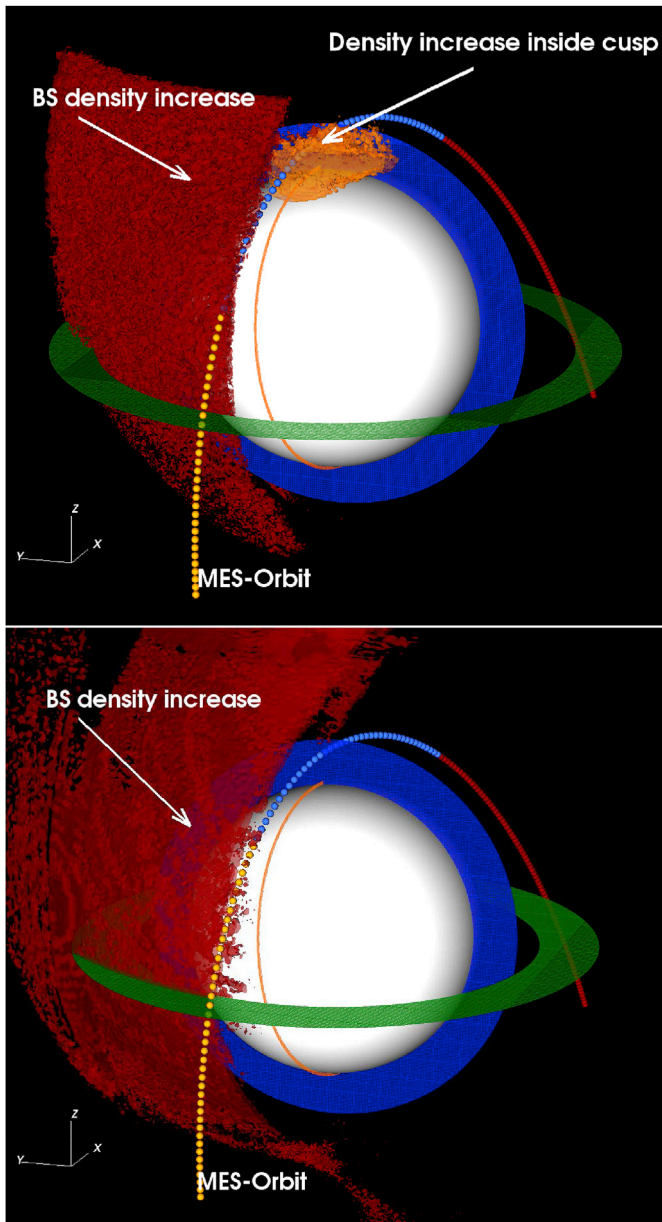


Fig. 4. Same description as Fig. 3 but plotting values of number densities where an increase of density at least 3.5 times above the background occurs (i.e., $n > 3.5n_0$). The density increase depicted in red is due to Mercury's bow-shock, whereas the density increase depicted in orange is due to the magnetopause cusp region.

aligned and has its maximum within a plane that can be identified as the (011)-plane in MASO-coordinates. Only about 10% of the total current flows perpendicular to the magnetic field. The 90% field aligned current connects to the high latitude polar currents that are plotted within the blue plane. The maximum current density of the field aligned currents is reached within the cusp-region where the reconnection rate is at its highest. However, the polar currents in the SU-case connect to the magnetopause currents in the equatorial regions, and not the polar regions as the SL-case.

4.2. 2D-section: parameters by Slavin et al. (2014)

We now restrict our analysis to the xy-plane and to the xz-plane of Mercury's interaction. This allows us to investigate structures near Mercury in more detail than in the three-dimensional figures discussed

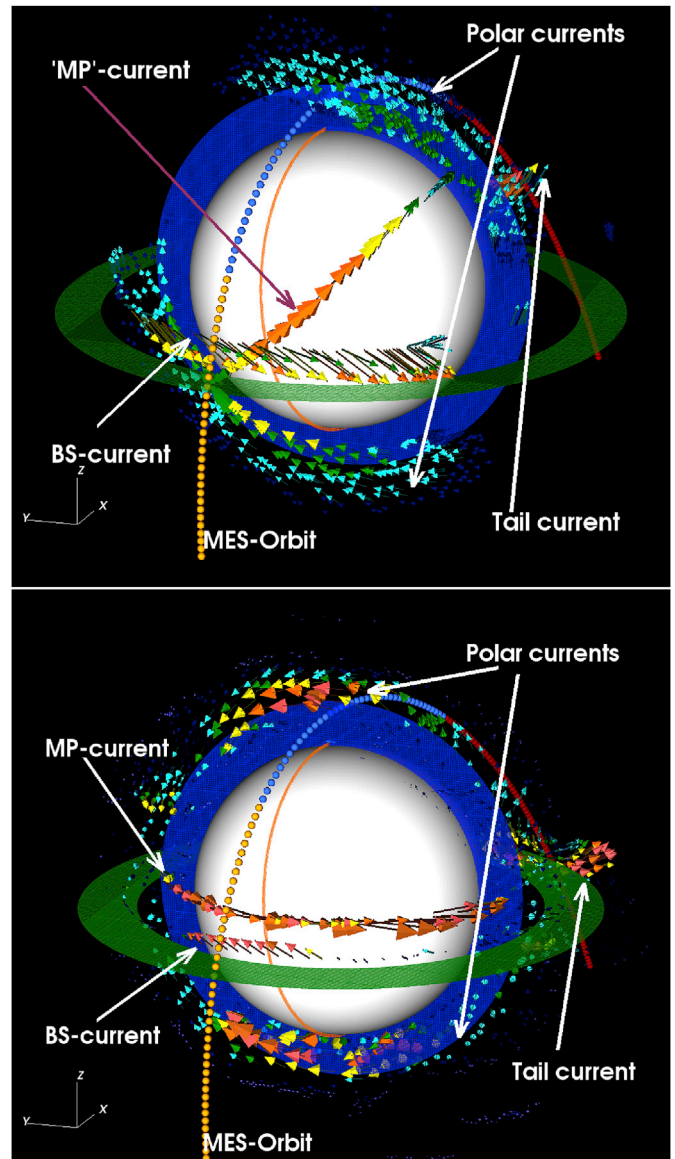


Fig. 5. Same description as Fig. 3 but with current vectors denoting the magnitude and direction of current systems within the bow-shock, magnetopause, and polar regions of Mercury's magnetosphere.

above. The xy-plane ($z=0$) and the orbital plane of MESSENGER (approximated by the xz-plane) of the SL-simulations are shown in Fig. 6(b) and (a) respectively. Number density in these planes are denoted by the green-to-red colorscale, whereas current density is displayed by the blue colorscale for currents above $J > 10^{-6} \text{ Am}^{-2}$. The projection of MESSENGER's orbit onto each plane is included. Normalized current vectors have been projected onto the respective planes to indicate local current directions. For a magnetic mach number of 2.5 and a ram pressure of 47 nPa (Slavin et al., 2014) a bow-shock distance of approximately $0.7R_M = 1708 \text{ km}$ and a magnetopause distance above the planet of $0.1R_M = 240 \text{ km}$ is estimated (using the Chapman-Ferraro sixth root dependence, Winslow et al. (2013)).

In Fig. 6(a), the tip of the bow-shock is shifted to $z = 0.2R_M$ consistent with the dipole offset, while having a stand-off distance of $0.45R_M = 1098 \text{ km}$ from Mercury's surface, which is closer than the value inferred by Slavin et al. (2014). This discrepancy can occur because of a different solar wind pressure, influence of higher (quadrupole) moments of Mercury's magnetic field or numerical smoothing within the simulation. The distance of the magnetopause is slightly closer, at

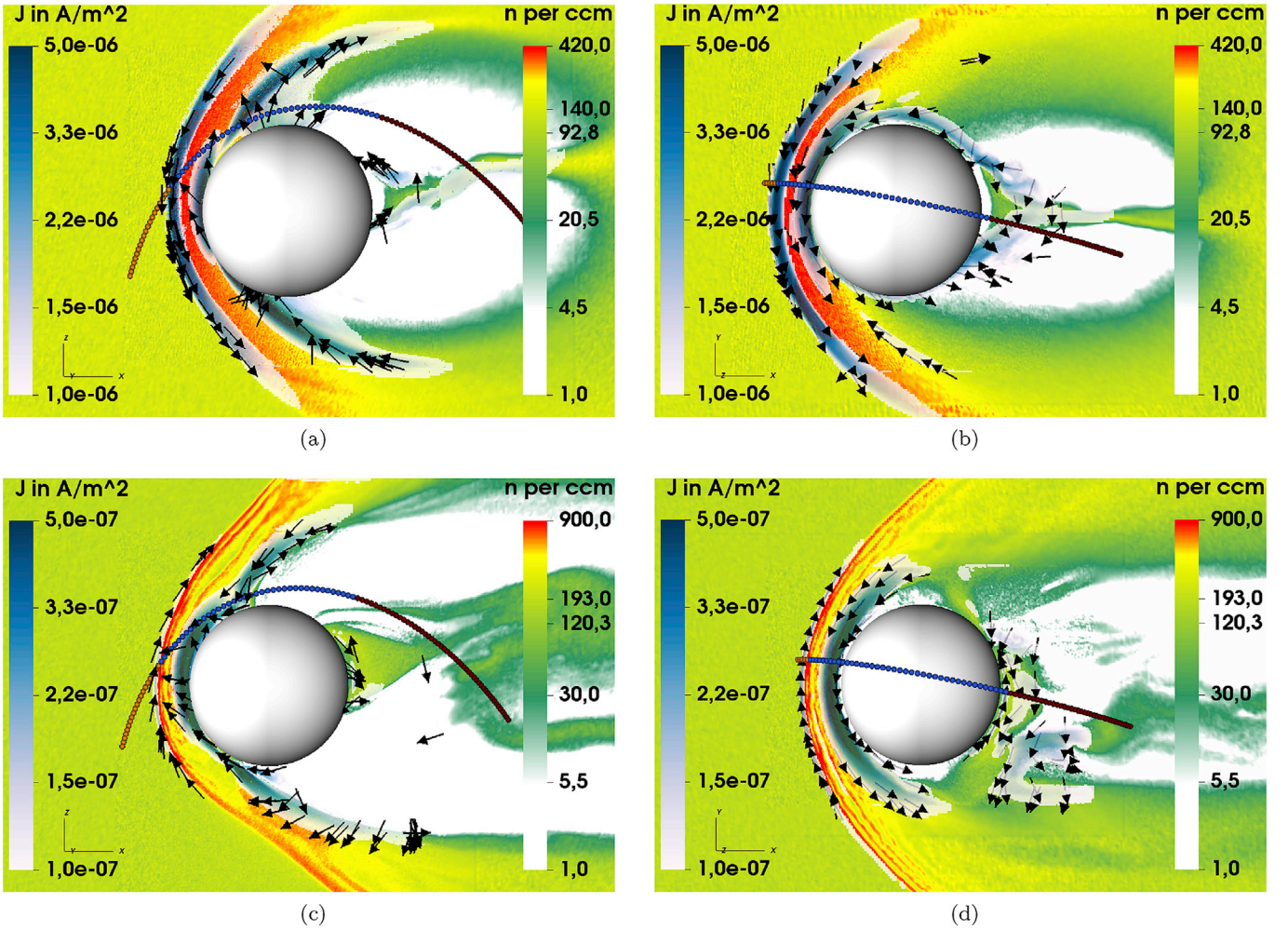


Fig. 6. A.I.K.E.F. simulation results of the two sets of plasma parameters, (a) and (b) show the Slavin-case, (c) and (d) the SUSANOO-case respectively. (a) and (c) show number and current densities in the xz -plane (approximately the MESSENGER orbital plane), while (b) and (d) display the xy -plane. The density is shown by the green-to-red colorscale while the overlaid current density is shown by the blue colorscale. Only current densities above $J > 10^{-6} \text{ Am}^{-2}$ (SL-case, panels a and b) and $J > 10^{-7} \text{ Am}^{-2}$ (SU-case, panels c and d) are shown. Current vectors (not to scale) are projected onto the respective planes to show the current flow directions. Note the decrease in current density by one order of magnitude from the SL-to the SU-case, and the difference in color scales between the two cases. The dotted line displays projection of the MESSENGER trajectory onto each plane.

$R_{MP} = 0.1R_M = 240 \text{ km}$. The particle density in the bow-shock increases to $2.85n_{0,SL} = 400 \text{ cm}^{-3}$ and keeps nearly constant until close to the surface with $n = 400 \text{ cm}^{-3}$ inside the magnetopause region. The plasma tail with a density of $n = 160 \text{ cm}^{-3}$ is shifted northward until it is parallel to the x -axis at $z = 0.8R_M$. Inside the cusp region the density reaches $n = 500 \text{ cm}^{-3}$ whereas the northern and southern lobes of the tail are completely devoid of solar wind particles. For a low mach number one would expect plasma depletion layers with a depth of $0.1R_{MP} = 24 \text{ km}$ (Gershman et al., 2013). However, the density depletion happens within $0.05R_M = 122 \text{ km}$ on the stagnation line within the simulation, a factor of 5 higher than the expected value. Since 24 km are below the grid resolution, its depth was therefore artificially extended and needs to be investigated by simulations that use a higher grid resolution or less numerical smoothing.

The bow-shock current density reaches $J = 6 \cdot 10^{-6} \text{ Am}^{-2}$ while the current density in the magnetopause region close to the surface is $J = 7 \cdot 10^{-6} \text{ Am}^{-2}$. The y -component of the current density is negative, and points out of the xz -plane. As seen in the global view in Fig. 5, only about $J = 7 \cdot 10^{-7} \text{ Am}^{-2}$ can be attributed to the magnetopause current perpendicular to the magnetic field. The parallel current part is used to close the narrower polar currents with a negative y -component. The northern current reaches $J = 6.5 \cdot 10^{-6} \text{ Am}^{-2}$ while flowing away from

the surface, while the southern current reaches $J = 8 \cdot 10^{-6} \text{ Am}^{-2}$ while flowing towards the surface. Current vectors in Fig. 6(b) show a current flow from the dawn-to dusk-side in the day-side region. The turning of the global magnetic field in Fig. 3 results in a bow-shock tip at $y = 0.2R_M$ within the xy -plane, as visible in Fig. 6(b). Solar wind particles flow around the dawn side, reproducing a similar particle flowing behavior as described by Müller et al. (2012). The neutral current sheet is inclined by $35\text{--}40^\circ$ from the xy -plane, and is therefore not encountered by MESSENGER until higher latitudes the SL-case.

4.3. 2D-section: parameters by SUSANOO

Hybrid model results using SU-parameters (representing the CME-phase) are shown in Fig. 6(c) and (d). In contrast to Fig. 6(a) and (b), current densities that exceed $J > 10^{-7} \text{ Am}^{-2}$ are shown. In the xz -plane the bow-shock is slightly closer to the surface of Mercury with a distance of $0.43R_M = 1050 \text{ km}$, while the magnetopause is at a distance of $0.115R_M = 280 \text{ km}$ on the x -axis and penetrates the surface in the southern latitudes, as a result of the high mach number. The magnetosheath region is filled with 3 density shocklets in the northern and 2 shocklet features in the southern bow-shock region. In contrast to the expected density increase at the bow-shock in ideal MHD by a factor of 4

(see, e.g., Kivelson and Russell (1995)), our hybrid model yields a density jump by a factor of $4.8 n_{0,SU}$ to $n = 960 \text{ cm}^{-3}$ because it considers kinetic effects. Furthermore, the shocklets reach a density peak of $n = 4.1 n_{0,SU} = 790 \text{ cm}^{-3}$. The plasma sheet is similarly spread but wider than the SL-case with a density of $n = 120 \text{ cm}^{-3}$. In the xy -plane, the dawn-side bow-shock has a 4th shocklet structure, showing again the more disturbed shape of the bow-shock region. Contrary to the SL-case, the night-side is more densely populated as more particles gyrate around Mercury.

The bow-shock current density reaches $J = 2.2 \cdot 10^{-7} \text{ Am}^{-2}$ while the magnetopause current is $J = 8.8 \cdot 10^{-7} \text{ Am}^{-2}$. The polar currents perpendicular to the field with a positive y -component can be affiliated with Chapman-Ferraro currents closed via the magnetopause currents. Their current densities reach up to $J = 4 \cdot 10^{-7} \text{ Am}^{-2}$ and $J = 9 \cdot 10^{-7} \text{ Am}^{-2}$ for the northern and southern parts respectively. The equatorial currents of bow-shock and magnetopause flow anti-parallel to each other, contrary to the parallel flow in the SL-case. The neutral current sheet is nearly equatorial but not clearly visible xy -($z = 0$)-plane as its maximum is focused within the xy -($z = 0.2R_M$)-plane. Thus

MESSENGER pierces the neutral current sheet closely to the equator.

4.4. 1D section: analysis of the simulation results along MESSENGER trajectory

The comparison of magnetic field data obtained by MESSENGER with our simulation output has been plotted in Fig. 7. MESSENGER data is shown in black, whereas our simulated models are in red (SL-case) and blue (SU-case). Additionally, we show a third simulation (depicted by the orange line in Fig. 7) with upstream conditions that use a linear average ((SL + SU)/2) of the SL- and SU-parameters displayed in Table 1. The x-axis shows the time in units of "day of year" (doy), with day 327 being 23 November 2011 and $0.01 \text{ doy} \approx 15 \text{ min}$. The MESSENGER data can be separated in 3 main segments: the northern tail lobe (until 327.415 doy), the northern polar region including the cusp region (between 327.415 doy and 327.43 doy) and the bow-shock region (at 327.44 doy). MESSENGER crossed the plasma sheet at 327.3925 doy where the x -component changed sign and the total magnetic field reached a minimum of $B = 45 \text{ nT}$. The total magnetic field then increased rapidly to 350 nT ,

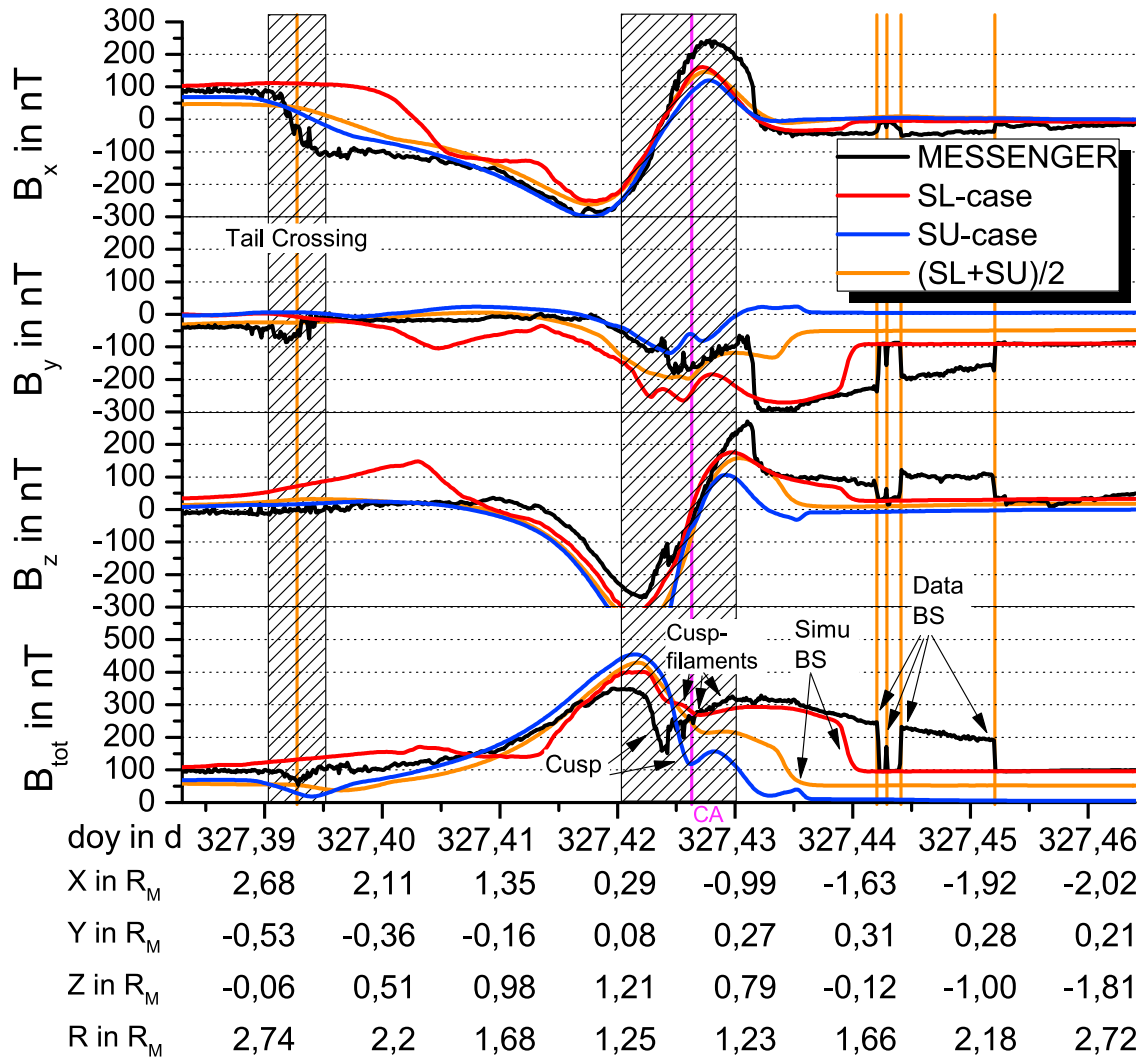


Fig. 7. Magnetic field measurements (black) compared to A.I.K.E.F. simulation results based of Slavin's (red) and SUSANNO's (blue) and with the average upstream conditions of the SL- and SU-parameters (orange) for the time interval between 327.39 doy \approx 09:21 UTC and 327.46 doy \approx 11:04 UTC of 23 November 2011 with $0.01 \text{ doy} \approx 15 \text{ min}$. The coordinates are displayed in the MASO system. The locations of bow-shocks, cusp, closest approach and tail crossing are labeled. Variations in the CME upstream parameters on the timescale of 15 min are likely to move the position of the bow-shock significantly (Winslow et al., 2013), as 4 bow-shock crossings could be measured. Numerical smoothing can move the position of bow-shock, plasma depletion layer and magnetopause within the simulations. See text for further discussion.

only to be followed by a sudden decrease of 200 nT and a furrowed increase to 300 nT, denoting the cusp region and cusp filaments (Slavin et al., 2014).

Between 327.4425 doy and 327.4525 doy, 4 bow-shock crossings can be identified. It is likely that within the CME, the alfvénic Mach number was lower than in the solar wind, resulting in a movement of the bow-shock location. This caused the bow-shock to overtake MESSENGER multiple times during this orbit (Slavin et al., 2014). Such an effect is consistent with a very disturbed solar wind, substantiated by the high disturbance index of 99.9 for this orbit (Anderson et al., 2013). Afterward, with a total magnetic field of 97 nT, the solar wind became calm and constant for a brief period of time. Those constant solar wind parameters have been described by Slavin et al. (2014) as representative for the whole provided data set and are included in Table 1.

Results of the hybrid simulation by the SL-parameters are included in Fig. 7 by the red line (SL-Case). The upstream solar wind magnetic field results are in agreement with the measurements upstream of Mercury around 327.46 doy. The simulation provides only one bow-shock crossing located about 4.3 min earlier than the final bow-shock crossing seen by MESSENGER. The simulation reproduces the bow-shock in jump strength by values of $B = 150$ nT. Also the bulge around 327.43 doy with a total magnetic field of $B = 300$ nT is replicated for the run with the SL-parameters. Yet differences up to 150 nT in the individual components of the magnetic field are visible. At all times before 327.43 doy, the modeled magnetic field data differs from the MESSENGER data, with neither the position nor magnitude of the cusp or tail crossing located at the observed position, and are each too weak compared to the measurements. Since the spacial scale of the cusp filaments is on the order of the grid resolution (Poh et al., 2016), they can not be resolved by our simulation.

The A.I.K.E.F. simulation with the SU-case data set, however, is able to reproduce the tail crossing at the observed time of 327.393 doy, yet underrepresents the magnitude by a field strength of $B = 75$ nT. The B_x and B_y components show close to perfect agreement with the MESSENGER data up to the cusp-region. B_z is in agreement until the spacecraft reaches closer distances to Mercury at 327.41 doy. From there, the negative z-component is up to 200 nT lower than MESSENGER measurements. At 327.427 doy the total magnetic field of the SU-case reaches a minimum of 100 nT followed by a 50 nT increase that is indicative of a cusp crossing. Even though the magnitude of the modeled B_y is smaller than observed by MESSENGER, both slopes are very similar and show that the cusp has only been grazed as was visible in the bottom panel of Fig. 3. Therefore the orbit in the SU-case only touches one side of the northern cusp and does not directly cross through the cusp as the MESSENGER data shows. The bow-shock is encountered at 327.435 doy with a much smaller increase of the magnetic field compared to the SL-case (only 40 nT versus 150 nT) which is approximately a factor of 7 increase from the upstream magnetic field of 5.5 nT. The depths of the magnetosheaths obtained by our A.I.K.E.F. simulations are 858 km and 800 km in the SL- and SU-Case respectively. These values are in agreement with the ranges from Winslow et al. (2013). An entire scan sequence of the Fast Imaging Plasma Spectrometer (FIPS) needs on the order of 11 min (Andrews et al., 2007). Therefore, it is likely that the inner magnetosphere density was affected by the impact of the CME and that the FIPS measurement from this timeframe may not be completely flawless. Additionally, note that the inclusion of a possible quadrupole term in Mercury's internal magnetic moment, a different upstream solar wind density or even a different amount of numerical smoothing can move the position of bow-shock and magnetopause significantly in the simulations.

Getting such agreement within the neutral sheet crossing region with the weak upstream magnetic field of the SU-parameters, show that the dominant magnetic field in the tail originates from Mercury's dipole. However, the appearance and direction of the neutral sheet current is still influenced by the upstream IMF direction.

Even though many of the features observed by MESSENGER upstream

and downstream of the cusp regions are explained by the two hybrid simulations, neither parameter set is able to generate a 200 nT decrease of the total magnetic field inside the cusp. Additionally, neither simulation is able to recreate the cusp filaments that were observed by MESSENGER, because of a too coarse grid resolution. The discrepancy between the modeled and measured B_x component can be attributed to closure currents flowing within the planetary interior to close the field-aligned-current system (Anderson et al., 2014). With the high disturbance index of Mercury's magnetosphere it is likely that in the time interval between the parameters represented by the SU- and SL-case, the upstream solar wind conditions evolved so violently that the bow-shock and cusp changed its size and position compared to the bow-shock's and cusp's size and location in the simulations. This hypothesis is supported by a third simulation where the upstream conditions are a linear average of the SL- and SU-parameters. Inside the upstream solar wind, the magnetic field is the direct average of SL- and SU-parameters, and the behavior in the magnetosphere is also within the range given by the red and blue line, except the short time before the tail crossing. Even though B_y in the cusp region shows very good agreement with the MESSENGER data, the modeled total magnetic field is lower than the MESSENGER observation in this region. Thus, even a simple linear interpolation of the solar wind parameters does not explain the cusp moving directly under MESSENGER's orbit. A very different temporary solar wind must therefore have taken place when MESSENGER was inside the cusp region to cause this observed feature. Because MESSENGER took 20 min between cusp region and first bow-shock crossing, and 10 min between first and last bow-shock crossings, we estimate a timescale for the CME variability on the order of 15 min. The CME obtained by the SUSANOO model yields a maximum magnetic field change of 10 nT over a two hour period within the CME-front, corresponding to a change of 1.25 nT every fifteen minutes. In comparison, the average change of the magnetic field within the rest of the simulated CME is only 2 nT every six hours. This is an extreme increase within time scales used in the SUSANOO model and suggests an even higher variability within the CME. As the actual change implied by our parameters used for the SL- and SU-Case is of 100 nT/1 hr, the SUSANOO model for this CME needs to be further improved. However, the good agreement of the SU-case simulation with the night side measurements of MESSENGER shows that the SUSANOO is a strong tool to predict upstream solar wind parameters at Mercury. Differences of the model to the CME are possibly due to uncertainties in the solar surface and corona observations, time and spacial resolutions and numerical smoothing.

5. Summary and conclusion

This study has presented hybrid simulations using inputs from a combination of MESSENGER observations (Slavin et al., 2014) and the SUSANOO MHD code Shiota and Kataoka (2016) to understand Mercury's magnetospheric response to an incoming CME on 23 November 2011.

The simulation show accurate agreement in the upstream solar wind regime (as they have been the SL-parameters) and correctly reproduces the bow-shock crossing with a jump in the total magnetic field by 150 nT. The day-side magnetosphere shows accordingly a magnetic field magnitude of 300 nT, yet, the modeled cusp and plasma sheet crossing have disparate magnetic field behavior than the MESSENGER data. Thus, the parameters obtained from Slavin et al. (2014) alone cannot be used to explain the whole data set of MESSENGER for that orbit.

Because of a Dungey-cycle time-scale of about 2 min, Mercury's magnetosphere reacts and adapts to new upstream solar wind conditions rapidly. Therefore, we are able to describe the magnetosphere during a CME passage piece-wise with our simulations. Recalculating the solar wind from within Mercury's magnetosphere on the night-side of the planet is challenging, so we used the MHD SUSANOO-SW model to simulate the CME and obtain upstream solar wind conditions.

With those parameters, we were able to find a good agreement with

MESSENGER data in the tail lobes, as the correct location of the plasma sheet crossing and the magnetic field behavior could be reproduced. It was shown that in the SU-case, the cusp moved in such a way that the orbit would have been able to cross this feature at the dawn-side. However, none of the simulations (SL-case, SU-case and a linear average of the two) were able to sufficiently move the cusp close enough to the spacecraft to create a full cusp crossing of MESSENGER. We can conclude that the solar wind inside the CME must be of high temporal variability within a time interval of 15 min to explain the observed movement of the cusp and the multiple bow-shock crossings that were observed by MESSENGER.

Acknowledgment

W.E. and U.M. acknowledge the North-German Supercomputing Alliance (HLRN) for providing HPC resources that have contributed to the research results reported in this paper. D.H. was supported by the German Ministerium für Wirtschaft und Energie and the German Zentrum für Luft-und Raumfahrt under contract 50 QW 1501. 3D and 2D plots were done with VisIt 2.10. (Childs et al., 2012). Source code of the hybrid model and complete results are available upon request.

Appendix A. Supplementary data

Supplementary data related to this article can be found at <https://doi.org/10.1016/j.pss.2017.12.016>.

References

- Anderson, B.J., Johnson, C.L., Korth, H., 2013. A magnetic disturbance index for Mercury's magnetic field derived from MESSENGER Magnetometer data. *G-cubed* 14 (9), 3875–3886.
- Anderson, B.J., Johnson, C.L., Korth, H., Purucker, M.E., Winslow, R.M., Slavin, J.A., Solomon, S.C., McNutt, R.L., Raines, J.M., Zurbuchen, T.H., Sep. 2011. The global magnetic field of mercury from MESSENGER orbital observations. *Science* 333 (6051), 1859–1862.
- Anderson, B.J., Johnson, C.L., Korth, H., Slavin, J.A., Winslow, R.M., Phillips, R.J., McNutt, R.L., Solomon, S.C., Nov 2014. Steady-state field-aligned currents at Mercury. *Geophys. Res. Lett.* 41 (21), 7444–7452. <http://doi.wiley.com/10.1002/2014GL061677>.
- Anderson, B.J., Johnson, C.L., Korth, H., Winslow, R.M., Borovsky, J.E., Purucker, M.E., Slavin, J. a., Solomon, S.C., Zuber, M.T., McNutt, R.L., 2012. Low-degree structure in Mercury's planetary magnetic field. *J. Geophys. Res. E: Planets* 117 (12), 1–17.
- Andrews, G.B., Zurbuchen, T.H., Mauk, B.H., Malcom, H., Fisk, L.A., Gloeckler, G., Ho, G.C., Kelley, J.S., Koehn, P.L., Lefevre, T.W., Livi, S.S., Lundgren, R.A., Raines, J.M., Aug. 2007. The energetic particle and plasma spectrometer instrument on the MESSENGER spacecraft. *Space Sci. Rev.* 131, 523–556.
- Baker, D.N., Odstreil, D., Anderson, B.J., Arge, C.N., Benna, M., Gloeckler, G., Korth, H., Mayer, L.R., Raines, J.M., Schriver, D., Slavin, J.A., Solomon, S.C., Trávníček, P.M., Zurbuchen, T.H., Dec. 2011. The space environment of Mercury at the times of the second and third MESSENGER flybys. *Planet. Space Sci.* 59, 2066–2074.
- Baker, D.N., Poh, G., Odstreil, D., Arge, C.N., Benna, M., Johnson, C.L., Korth, H., Gershman, D.J., Ho, G.C., McClintock, W.E., Cassidy, T.A., Merkel, A., Raines, J.M., Schriver, D., Slavin, J.A., Solomon, S.C., Trávníček, P.M., Winslow, R.M., Zurbuchen, T.H., Jan. 2013. Solar wind forcing at Mercury: WSA-ENLIL model results. *J. Geophys. Res. Space Phys.* 118, 45–57.
- Benna, M., Anderson, B.J., Baker, D.N., Boardsen, S.A., Gloeckler, G., Gold, R.E., Ho, G.C., Killen, R.M., Korth, H., Krimigis, S.M., Purucker, M.E., McNutt, R.L., Raines, J.M., McClintock, W.E., Sarantos, M., Slavin, J.A., Solomon, S.C., Zurbuchen, T.H., 9 2010. Modeling of the magnetosphere of mercury at the time of the first MESSENGER flyby. *Icarus* 209 (1), 3–10.
- Childs, H., Brugger, E., Whitlock, B., Meredith, J., Ahern, S., Pugmire, D., Biagas, K., Miller, M., Harrison, C., Weber, G.H., Krishnan, H., Fogal, T., Sanderson, A., Garth, C., Bethel, E.W., Camp, D., Rübél, O., Durant, M., Favre, J.M., Navrátil, P., Oct 2012. VisIt: an end-user tool for visualizing and analyzing very large data. In: *High Performance Visualization—Enabling Extreme-Scale Scientific Insight*, pp. 357–372.
- Christensen, U.R., Dec. 2006. A deep dynamo generating Mercury's magnetic field. *Nature* 444, 1056–1058.
- Feyerabend, M., Simon, S., Neubauer, F.M., Motschmann, U., Bertucci, C., Ederberg, N.J.T., Hospodarsky, G.B., Kurth, W.S., Jan. 2016. Hybrid simulation of Titan's interaction with the supersonic solar wind during Cassini's T96 flyby. *Geophys. Res. Lett.* 43, 35–42.
- Gershman, D.J., Slavin, J.A., Raines, J.M., Zurbuchen, T.H., Anderson, B.J., Korth, H., Baker, D.N., Solomon, S.C., Nov. 2013. Magnetic flux pileup and plasma depletion in Mercury's subsolar magnetosheath. *J. Geophys. Res. Space Phys.* 118, 7181–7199.
- Glassmeier, K.-H., Auster, H.-U., Motschmann, U., Nov. 2007. A feedback dynamo generating Mercury's magnetic field. *Geophys. Res. Lett.* 34, 22201.
- Hauck, S.A., Margot, J.-L., Solomon, S.C., Phillips, R.J., Johnson, C.L., Lemoine, F.G., Mazarico, E., McCoy, T.J., Padovan, S., Peale, S.J., Perry, M.E., Smith, D.E., Zuber, M.T., Jun. 2013. The curious case of Mercury's internal structure. *J. Geophys. Res. (Planets)* 118, 1204–1220.
- Herčík, D., Trávníček, P.M., Johnson, J.R., Kim, E.-H., Hellinger, P., Jan. 2013. Mirror mode structures in the asymmetric Hermean magnetosheath: hybrid simulations. *J. Geophys. Res. Space Phys.* 118, 405–417.
- Heyner, D., Wicht, J., Gómez-Pérez, N., Schmitt, D., Auster, H.-U., Glassmeier, K.-H., Dec. 2011. Evidence from numerical experiments for a feedback dynamo generating Mercury's magnetic field. *Science* 334, 1690–1702.
- Jia, X., Slavin, J.A., Gombosi, T.I., Daldorff, L.K.S., Toth, G., Holst, B., Jun. 2015. Global MHD simulations of Mercury's magnetosphere with coupled planetary interior: induction effect of the planetary conducting core on the global interaction. *J. Geophys. Res. Space Phys.* 120, 4763–4775.
- Jia, Y.-D., Ma, Y.J., Russell, C.T., Lai, H.R., Toth, G., Gombosi, T.I., Apr. 2012. Perpendicular flow deviation in a magnetized counter-streaming plasma. *Icarus* 218, 895–905.
- Johnson, C.L., Philpott, L.C., Anderson, B.J., Korth, H., Hauck, S.A., Heyner, D., Phillips, R.J., Winslow, R.M., Solomon, S.C., Mar. 2016. MESSENGER observations of induced magnetic fields in Mercury's core. *Geophys. Res. Lett.* 43, 2436–2444.
- Kivelson, M.G., Russell, C.T., Apr. 1995. *Introduction to Space Physics*. Cambridge University Press.
- Koenders, C., Glassmeier, K.-H., Richter, I., Ranocha, H., Motschmann, U., Jan. 2015. Dynamical features and spatial structures of the plasma interaction region of 67P/Churyumov-Gerasimenko and the solar wind. *Planet. Space Sci.* 105, 101–116.
- Korth, H., Anderson, B.J., Zurbuchen, T.H., Slavin, J.A., Perri, S., Boardsen, S.A., Baker, D.N., Solomon, S.C., McNutt, R.L., Dec. 2011. The interplanetary magnetic field environment at Mercury's orbit. *Planet. Space Sci.* 59, 2075–2085.
- Kriegel, H., Simon, S., Meier, P., Motschmann, U., Saur, J., Wennmacher, A., Strobel, D.F., Dougherty, M.K., 2014. Ion densities and magnetic signatures of dust pick-up at Enceladus. *J. Geophys. Res.: Space Pol.* 119 (4), 2740–2774.
- Liuzzo, L., Simon, S., Feyerabend, M., Motschmann, U., Sep 2016. Disentangling plasma interaction and induction signatures at callisto: the galileo c10 flyby. *J. Geophys. Res. Space Pol.* 121 (9), 8677–8694.
- Müller, J., Simon, S., Motschmann, U., Schüle, J., Glaßmeier, K.-H., Pringle, G.J., 4 2011. A.i.k.e.f.: adaptive hybrid model for space plasma simulations. *Comput. Phys. Commun.* 182 (4), 946–966.
- Müller, J., Simon, S., Wang, Y.-C., Motschmann, U., Heyner, D., Schüle, J., Ip, W.-H., Kleindienst, G., Pringle, G.J., 3 2012. Origin of Mercury's double magnetopause: 3D hybrid simulation study with A.I.K.E.F. *Icarus* 218, 666–687.
- Poh, G., Slavin, J.A., Jia, X., DiBraccio, G.A., Raines, J.M., Imber, S.M., Gershman, D.J., Sun, W.-J., Anderson, B.J., Korth, H., Zurbuchen, T.H., McNutt, R.L., Solomon, S.C., Sep. 2016. MESSENGER observations of cusp plasma filaments at Mercury. *J. Geophys. Res. Space Phys.* 121, 8260–8285.
- Raines, J.M., Slavin, J.A., Zurbuchen, T.H., Gloeckler, G., Anderson, B.J., Baker, D.N., Korth, H., Krimigis, S.M., McNutt, R.L., Dec. 2011. MESSENGER observations of the plasma environment near Mercury. *Planet. Space Sci.* 59, 2004–2015.
- Shiota, D., Kataoka, R., Feb. 2016. Magnetohydrodynamic simulation of interplanetary propagation of multiple coronal mass ejections with internal magnetic flux rope (SUSANOO-CME). *Space Weather* 14, 56–75.
- Shiota, D., Kataoka, R., Miyoshi, Y., Hara, T., Tao, C., Masunaga, K., Futaana, Y., Terada, N., Apr. 2014. Inner heliosphere MHD modeling system applicable to space weather forecasting for the other planets. *Space Weather* 12 (4), 187–204.
- Slavin, J.A., Acuña, M.H., Anderson, B.J., Baker, D.N., Benna, M., Boardsen, S.A., Gloeckler, G., Gold, R.E., Ho, G.C., Korth, H., Krimigis, S.M., McNutt, R.L., Raines, J.M., Sarantos, M., Schriver, D., Solomon, S.C., Trávníček, P., Zurbuchen, T.H., May 2009. MESSENGER observations of magnetic reconnection in Mercury's magnetosphere. *Science* 324, 606.
- Slavin, J.A., Anderson, B.J., Baker, D.N., Benna, M., Boardsen, S.A., Gloeckler, G., Gold, R.E., Ho, G.C., Korth, H., Krimigis, S.M., McNutt, R.L., Nittler, L.R., Raines, J.M., Sarantos, M., Schriver, D., Solomon, S.C., Starr, R.D., Trávníček, P.M., Zurbuchen, T.H., Aug. 2010. MESSENGER observations of extreme loading and unloading of Mercury's magnetic tail. *Science (New York, N.Y.)* 329 (5992), 665–668.
- Slavin, J.A., Anderson, B.J., Baker, D.N., Benna, M., Boardsen, S.A., Gold, R.E., Ho, G.C., Imber, S.M., Korth, H., Krimigis, S.M., McNutt Jr., R.L., Raines, J.M., Sarantos, M., Schriver, D., Solomon, S.C., Trávníček, P., Zurbuchen, T.H., Jan. 2012. MESSENGER and Mariner 10 flyby observations of magnetotail structure and dynamics at Mercury. *J. Geophys. Res. Space Phys.* 117, 1215.
- Slavin, J.A., DiBraccio, G.A., Gershman, D.J., Imber, S.M., Poh, G.K., Raines, J.M., Zurbuchen, T.H., Jia, X., Baker, D.N., Glassmeier, K.-H., Livi, S.A., Boardsen, S.A., Cassidy, T.A., Sarantos, M., Sundberg, T., Masters, A., Johnson, C.L., Winslow, R.M., Anderson, B.J., Korth, H., McNutt, R.L., Solomon, S.C., Oct. 2014. MESSENGER observations of Mercury's dayside magnetosphere under extreme solar wind conditions. *J. Geophys. Res. Space Phys.* 119, 8087–8116.
- Smith, D.E., Zuber, M.T., Phillips, R.J., Solomon, S.C., Hauck, S.A., Lemoine, F.G., Mazarico, E., Neumann, G.A., Peale, S.J., Margot, J.-L., Johnson, C.L., Torrence, M.H., Perry, M.E., Rowlands, D.D., Goossens, S., Head, J.W., Taylor, A.H., Apr. 2012. Gravity field and internal structure of mercury from MESSENGER. *Science* 336, 214.
- Stanley, S., Bloxham, J., Hutchison, W.E., Zuber, M.T., May 2005. Thin shell dynamo models consistent with Mercury's weak observed magnetic field [rapid communication]. *Earth Planet Sci. Lett.* 234, 27–38.
- Trávníček, P.M., Schriver, D., Hellinger, P., Herčík, D., Anderson, B.J., Sarantos, M., Slavin, J.A., Sep. 2010. Mercury's magnetosphere-solar wind interaction for northward and southward interplanetary magnetic field: hybrid simulation results. *Icarus* 209, 11–22.

- Vernisse, Y., Riousset, J., Motschmann, U., Glassmeier, K.-H., Mar 2017. Simulations of stellar winds and planetary bodies: ionosphere-rich obstacles in a super-alfvénic flow. *Planet. Space Sci.* 137, 64–72.
- Wang, Y.-C., Mueller, J., Motschmann, U., Ip, W.-H., Sep. 2010. A hybrid simulation of Mercury's magnetosphere for the MESSENGER encounters in year 2008. *Icarus* 209, 46–52.
- Winslow, R.M., Anderson, B.J., Johnson, C.L., Slavin, J.A., Korth, H., Purucker, M.E., Baker, D.N., Solomon, S.C., May 2013. Mercury's magnetopause and bow shock from MESSENGER Magnetometer observations. *J. Geophys. Res. Space Phys.* 118 (5), 2213–2227. <https://doi.org/10.1002/jgra.50237>.
- Yashiro, S., 2004. A catalog of white light coronal mass ejections observed by the SOHO spacecraft. *J. Geophys. Res.* 109 (A7).